

Cadmium Zinc Telluride Detectors for a Next-Generation Hard X-ray Telescope

J. Tang^{a,*}, F. Kislat^b, H. Krawczynski^a

^aWashington University in St. Louis, Physics Department, 1 Brookings Dr., CB 1105, St. Louis, MO 63130

^bUniversity of New Hampshire, Department of Physics & Astronomy and Space Science Center, 8 College Rd, Durham, NH 03824

Abstract

We are currently developing Cadmium Zinc Telluride (CZT) detectors for a next-generation space-borne hard X-ray telescope which can follow up on the highly successful *NuSTAR* (Nuclear Spectroscopic Telescope Array) mission. Since the launch of *NuSTAR* in 2012, there have been major advances in the area of X-ray mirrors, and state-of-the-art X-ray mirrors can improve on *NuSTAR*'s angular resolution of ~ 1 arcmin Half Power Diameter (HPD) to $15''$ or even $5''$ HPD. Consequently, the size of the detector pixels must be reduced to match this resolution. This paper presents detailed simulations of relatively thin (1 mm thick) CZT detectors with hexagonal pixels at a next-neighbor distance of $150\ \mu\text{m}$. The simulations account for the non-negligible spatial extent of the deposition of the energy of the incident photon, and include detailed modeling of the spreading of the free charge carriers as they move toward the detector electrodes. We discuss methods to reconstruct the energies of the incident photons, and the locations where the photons hit the detector. We show that the charge recorded in the brightest pixel and six adjacent pixels suffices to obtain excellent energy and spatial resolutions. The simulation results are being used to guide the design of a hybrid application-specific integrated circuit (ASIC)-CZT detector package.

Keywords: High energy X-ray astrophysics, Instrumentation, Solid state detectors, CZT, Detectors

1. Introduction

Cadmium Zinc Telluride (CZT) detectors are an attractive detector technology for hard X-ray astronomy as they offer excellent spatial resolutions, good energy resolutions, and, compared to Si and Ge detectors, much larger photoelectric effect cross sections at hard X-ray energies. A CZT imager may be used on a next-generation telescope succeeding the space-based hard X-ray telescope *NuSTAR* (Harrison et al., 2013). The high stopping power and excellent energy resolution of the *NuSTAR* CZT detectors enabled it to image the Cassiopeia A (Cas A) supernova remnant in the 67.9 keV and 78.4 keV line emissions from the radioactive isotope ^{44}Ti (Grefenstette et al., 2014; Boggs et al., 2015; Grefenstette et al., 2017). Contrary to the soft X-ray lines detected previously, the nuclear ^{44}Ti emission directly tracks the yield of nuclear material independent of the temperature and density of the ejecta (Grefenstette et al., 2014; Boggs et al., 2015; Grefenstette et al., 2017).

The recently developed monocrystalline silicon X-ray mirrors (Zhang et al., 2018) or electro-formed-nickel replicated (ENR) X-ray optics (Gaskin et al., 2015) promise angular resolutions with Half Power Diameters (HPD) of between a few arcseconds and 15 arcseconds – even at hard X-ray energies. The proposed *HEX-P* (Madsen et al., 2018) and *BEST* (Krawczynski et al., 2012) observatories seek to capitalize on this technology, as the point source sensitivity scales linearly with the angular resolution. Nyquist sampling the images provided by the improved X-ray mirrors requires detectors with excellent spatial

resolutions. Our group is thus leading the development of new small-pixel CZT detectors with center-to-center pitch of 150 microns and hexagonal pixels, improving by a factor of four over *NuSTAR*'s CZT detectors (605-micron pixel pitch).

This paper discusses the simulations performed for the design of the third-generation Hyperspectral Energy-resolving X-ray Imaging Detector (HEXID3 Li et al., 2017, 2018), which features hexagonal pixels at a next-neighbor pitch of $\sim 150\ \mu\text{m}$ and uses a low noise front end design achieving a projected readout noise of 14 electrons Root Mean Square (RMS). The advantage of using hexagonal over square pixels is that all the nearest neighbors of any given pixel are equivalent; in square pixels, some immediate neighbors are closer than others. Another similar ASIC for hybridization with pixelated CZT detectors is the High Energy X-ray Imaging Technology (HEXITEC) ASIC developed by Rutherford Appleton Laboratory. The HEXITEC ASIC features 6400 square pixels at a next-neighbor pitch of $250\ \mu\text{m}$ with an electronic readout noise of 50 electrons RMS (Ryan et al., 2016; Baumgartner et al., 2016; Ryan et al., 2017).

Our simulations model in detail the interactions of the incident photons, secondary photons and high-energy electrons generated in the CZT, and the ionization losses of the latter. The simulations furthermore model the drift and diffusion of the negative and positive charge carriers through the CZT, including the effects of mutual repulsion of charge carriers of equal polarity. This detailed treatment allows us to predict the properties of the signals, including the pixel multiplicity, and the dependence of the pixel signals on where in the detector the free charge carriers are generated. Earlier discussions of CZT de-

*Corresponding author

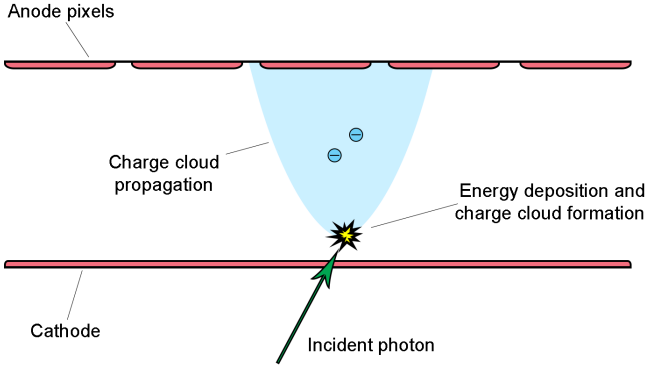


Figure 1: Sketch showing how an energy deposition leads to the generation of a free electron cloud that follows the applied electric field to the anode contacts, and widens owing to the effects of diffusion and repulsion of charges of equal polarity. Our model captures the effects of charge carriers being created along one or sometimes several photo-electron tracks, and accounts not only for drifting electrons (shown here), but also for drifting holes (not shown).

tector simulations can be found in (Benoit and Hamel, 2009; Kitaguchi et al., 2011; Ryan et al., 2017; Persson and Pelc, 2019; Lai et al., 2019). Compared to the earlier study of small pixel detectors of (Ryan et al., 2017), the shape of our charge clouds evolve owing to charge carrier repulsion and diffusion as the clouds drift inside the detector. Furthermore, we extend the study from a pixel pitch of $250\ \mu\text{m}$ to smaller $150\ \mu\text{m}$ pixels.

The rest of the paper is organized as follows. After describing the detector simulation methodology in Section 2, we present the results of the simulations in Section 3. Our studies show that the 1 mm thick detectors have a limited energy range over which they give excellent performance. We discuss the results and implications for the camera of a *NuSTAR* follow-up mission in Section 4.

2. Simulations of the CZT/ASIC Hybrid Detectors

X-rays impinging on a CZT detector interact via photoelectric, scattering, and pair production interactions. Photoelectric interactions dominate up to primary photon energies of $E_\gamma < 240\ \text{keV}$ at which Compton scattering becomes dominant (assuming 40% Cd, 10% Zn and 50% Te). The photo-electron of a photoelectric effect interaction loses most of its energy to ionization. The ionization promotes electrons to the conduction band, generating clouds of electrons and holes. Applying a bias across the detector causes the charge carriers to drift and to induce the read-out signal. While drifting, the charge clouds expand due to the repulsion and attraction between charge carriers and diffuse owing to spatial concentration gradients. In small-pixel detectors, the charge clouds can spread and induce currents over multiple pixels, resulting in charge sharing (Fig. 1).

The simulations consist of three parts: simulations of the photon interaction and subsequent energy losses of the photo-electron, Compton electron, or produced pairs and their secondaries, a simulation of the detector drift field, and charge cloud tracking and signal integration.

2.1. Geant4 Simulations

The interaction of the photons with the 1 mm thick detector are simulated with the Geant4 simulation toolkit (CERN, 2019) at discrete photon energies. The resulting interactions and energy depositions are stored for subsequent post-processing.

The upper panel of Figure 2 shows the energies deposited in the simulated CZT detector by a beam of 50 keV photons. A large fraction of 89.3% of the photons deposit their full energy in the detector. Some prominent escape peaks can be recognized. The peaks correspond to the initial energy of 50 keV minus the fluorescence photon energies. Secondary photons from an earlier interaction may escape the detector, resulting in incomplete energy detection, as shown by the energy depositions less than 50 keV. The lower panel of Figure 2 shows the energy of the photons produced in the CZT and identifies several prominent X-ray lines of the Cd, Zn, and Te atoms. The objective of the optimization of the detector design is to reconstruct the deposited energy as well as possible. The energy escaping the detector can, of course, not be recovered, and thus contributes along the Fano factor limit to the theoretical best possible achievable energy resolution.

2.2. Potential Simulations

The electrostatic potential ϕ and electric field inside the detector are inferred from solving Gauss' law with Dirichlet boundary conditions:

$$\nabla \cdot \mathbf{D} = -\nabla \epsilon \cdot \nabla \phi - \epsilon \nabla^2 \phi = 0. \quad (1)$$

Here, \mathbf{D} is the electric displacement field, and $\epsilon \approx 10\epsilon_0$ is the electric permittivity of CZT (Kitaguchi et al., 2011). Eq. (1) is solved on a three-dimensional discrete rectangular grid. The detector has a monolithic cathode in the $z = 0$ plane and a hexagonally-pixelated anode at the $z = d$ plane, where d is the thickness of the detector. The x and y directions are equivalent in terms of the grid resolution needed, so we set $\delta x = \delta y \neq \delta z$, where δx , δy , and δz denote the grid spacing in the x , y , and z directions, respectively. We expect the potential to closely resemble that of a parallel plate capacitor throughout most of the detector, so we take δz to be relatively large compared to δx and δy . We use the finite difference approximations

$$\frac{df}{dx} = \frac{f(x+h) - f(x-h)}{2h} + O(h^2), \quad (2)$$

$$\frac{d^2f}{dx^2} = \frac{f(x+h) - 2f(x) + f(x-h)}{h^2} + O(h^2) \quad (3)$$

to solve Eq. (1) with the Successive Overrelaxation Method (SOR) (Press et al., 2007). In each iteration, the electric potential is updated to the average of the surrounding values, including a certain amount of ‘‘overshooting’’ to accelerate convergence:

$$\phi \mapsto \omega \phi^* + (1 - \omega)\phi, \quad (4)$$

where ω is called the overrelaxation factor and ϕ^* is calculated by solving for the potential at the center grid point after substituting Eqs. (2) and (3) into Eq. (1). The method converges for

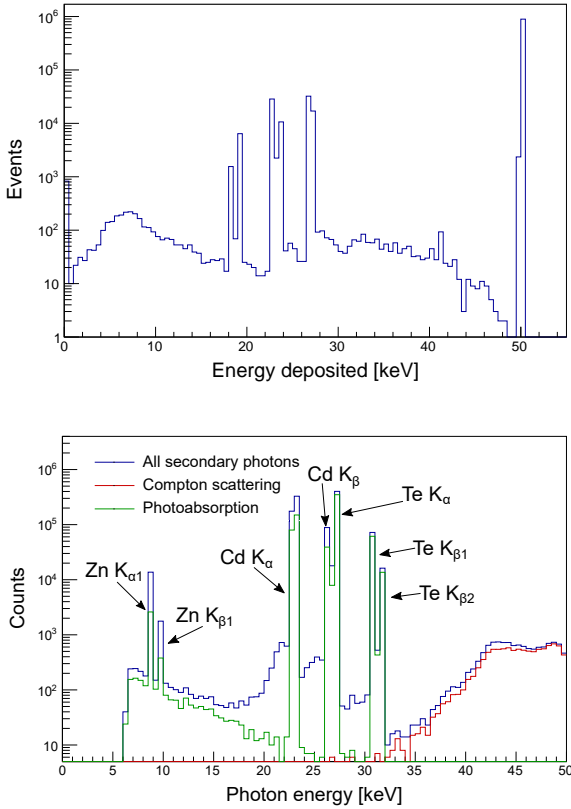


Figure 2: *Top*: Distribution of the total energy deposited by 50 keV photons in the CZT detectors. In this simulation of 10^6 events, 89.3% have the full 50 keV deposited. For the remaining events, some energy escapes the detector, leading to substantially smaller total energy deposits. *Bottom*: For the same incident 50 keV photons as shown in the upper panel, the lower panel presents the distribution of the energies of photons produced in the CZT detector, either through Compton scattering, or, following photoelectric absorption and the inelastic scattering of the photo-electron, through the emission of fluorescent photons. Prominent fluorescence lines are labeled.

values of ω between 1 and 2. The running time can be reduced by starting with an initial guess that is close to the expected potential. The final potential is expected to be close to that of a parallel plate capacitor, so the starting configuration was a simple gradient in z .

The error is calculated using the norm of an error vector \mathbf{e} , where $e_i = (\nabla \cdot \mathbf{D})_i$, where $(\nabla \cdot \mathbf{D})_i$ ($\nabla \cdot \mathbf{D}$ calculated at the i^{th} grid point) is calculated using Eq. (1) and the discrete derivatives. For a tolerance ε and G grid points, we consider the simulation converged if $|\mathbf{e}| < \varepsilon G$. For our simulations, we chose a tolerance of 10^{-6} .

This paper presents the results of simulations for a single detector geometry as described by Table 1. We use periodic boundary conditions in the x and y directions and a grounded plane beyond the anode at $z = 2d$, where d is the detector thickness. The last boundary condition is imposed to simulate the potential inside and outside of the detector so that the electric field between pixels can be calculated. The results for this simulation are shown in Fig. 3.

2.3. Charge Tracking and Integration

For each event, the Geant4 simulations give us the locations of the ionization energy deposits in the detector, which we offset to randomize the incident photon over a rectangular unit cell centered on a single pixel. We use this information to generate electrons and holes that are free to move through the detector. Energy depositions which occur sufficiently close to one another are merged and treated as a single deposition (discussed further in 2.3.2) while unmerged depositions are treated independently.

Subsequently, we track the motion of these electrons and holes through the detector accounting for the local electric field (caused by the applied detector bias), as well as charge carrier diffusion (a stochastic process) and electron-electron repulsion. We group charge carriers into small bundles (also referred to in this paper as “charge elements”) which are tracked as a single unit, with electron and hole bundles being pulled in opposite directions by the local electric field, and individual charge bundles experiencing different diffusion and repulsion related displacements. The photo-electrons of some events cause the emission of fluorescent photons, that, when being absorbed, give rise to secondary photo-electrons. Our treatment allows us to track the free charge carriers from all these processes.

2.3.1. Carrier Drift

We evolve the drift velocity with the equation

$$\mathbf{v}_d = \pm \mu \mathbf{E} = \mp \mu \nabla \phi, \quad (5)$$

where μ is the carrier mobility and is defined to be positive for both electrons and holes. The upper signs are for holes and the lower signs are for electrons. Table 1 lists the mobilities used in the simulations with subscripts e and h for electrons and holes, respectively. We calculate the electric field at the grid points as described above and use a trilinear interpolation to calculate the electric field between grid points. The resulting change in position per integration step is calculated using Euler’s method: $\delta \mathbf{r} = \mathbf{v}_d \delta t$.

2.3.2. Diffusion and Repulsion

We implement the expansion of a carrier cloud through diffusion and repulsion following Benoit and Hamel (Benoit and Hamel, 2009). We neglect the attraction between charge carriers of opposite polarity, which may slow down the initial charge separation. For an energy deposition E_d and mean ionization energy per electron hole pair \mathcal{E} , an average of $N_0 = E_d/\mathcal{E}$ electron-hole pairs are created. The actual number of electron-hole pairs created N is chosen from a Gaussian distribution with mean N_0 and $\sigma = \sqrt{N_0 F}$, where F is the Fano factor. For CZT, this is $F = 0.089$ (Table 1). To improve performance, the cloud of N charge carriers is broken down into n charge elements, each containing N/n charge carriers. The initial distribution of these charge elements is modeled by a spherically symmetric Gaussian with RMS radius

$$R_p = AE_d \left(1 - \frac{B}{1 + CE_d} \right), \quad (6)$$

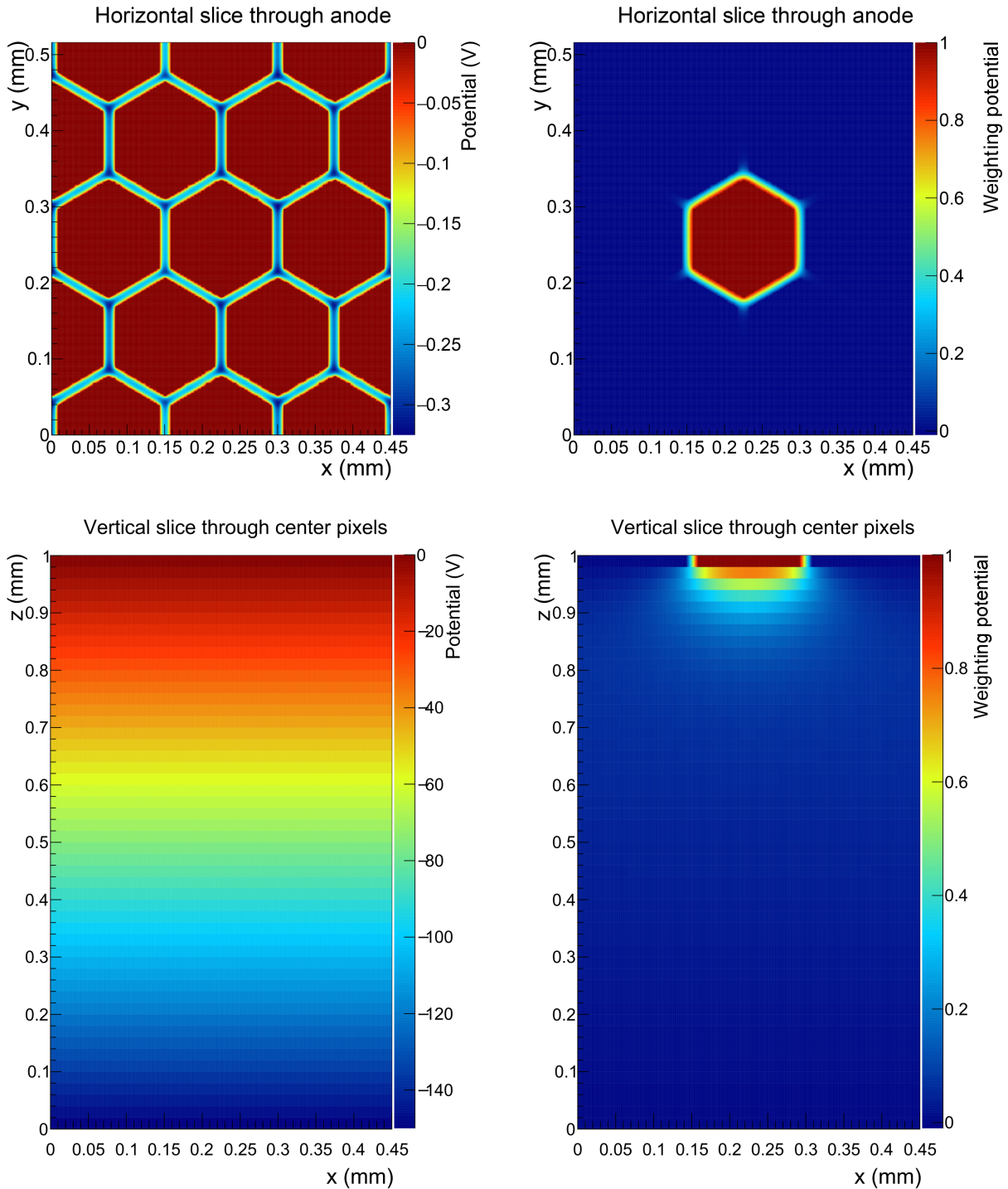


Figure 3: Two-dimensional slices of the three-dimensional simulated potentials. This geometry features a 1 mm thick detector, 150 μm center-to-center pitch with 15 μm spacing between pixels, and a -150 V bias. The bottom slices (vertical slices through the center pixels) only show the potential inside the detector; however, there is additional vacuum simulated up to $z = 2\text{ mm}$, at which there is a grounded plane. This serves as the upper boundary condition. *Left:* Slices of the electric potential. This is the drift field which pulls electrons toward the pixelated anode side and holes towards the cathode side of the detector. *Right:* Slices of the weighting potential. This is the field that is integrated along the carriers' trajectories to calculate the induced signal.

Simulation parameter	Symbol	Value	Reference
Grid spacing in x, y	$\delta x = \delta y$	1/750 mm	Kitaguchi et al. (2011)
Grid spacing in z	δz	1/50 mm	
Dielectric constant	ϵ	10 ϵ_0	
Time step	δt	0.5 ns	
Mean ionization energy	\mathcal{E}	4.6 eV	
Fano factor	F	0.089	
Electron mobility	μ_e	1000 cm ² /V · s	
Electron trapping time	τ_e	2.7 μ s	
Hole mobility	μ_h	110 cm ² /V · s	
Hole trapping time	τ_h	1.6 μ s	
Electron diffusion constant	D_e	26 cm ² /s	
Hole diffusion constant	D_h	3 cm ² /s	
Detector thickness	–	1 mm	
Pixel pitch	–	150 μ m	
Pixel spacing	–	15 μ m	
Cathode bias	–	–150 V	

Table 1: Constants and detector parameters for the simulation.

where $A = 0.95 \mu\text{m}/\text{keV}$, $B = 0.98$, and $C = 0.003 \text{keV}^{-1}$ are material-specific constants (Wohl et al., 1984). In our simulations, this is not only used to parameterize the initial charge distribution, but it is also used to determine whether two clouds are close enough to affect each others' diffusion and repulsion, in which case the energy depositions are merged and the two clouds are approximated by a single cloud located at the center of mass. The merging criteria was determined based on observations of the degree to which charge clouds expanded from the initial distribution in the same simulations.

The density gradient within a cloud causes diffusion of the charge elements and the electric field created by the charges causes repulsion. These affect the charge density ρ according to

$$\frac{\partial \rho}{\partial t} = D \nabla^2 \rho - \mu \nabla \cdot (\rho \mathbf{E}), \quad (7)$$

where D is the diffusion coefficient, μ is the carrier mobility, and \mathbf{E} here is the electric field produced by the charges in the cloud (Benoit and Hamel, 2009). The values of D used in our simulation for electrons and holes are listed in 1 with subscripts e and h , respectively, and were derived using the Einstein relation for charged particles at room temperature:

$$D = \frac{\mu k_B T}{q}. \quad (8)$$

Benoit and Hamel showed that for an ellipsoidal Gaussian charge distribution with $\boldsymbol{\sigma} = (\sigma_x, \sigma_y, \sigma_z)$, the time evolution of the distribution is described by

$$\frac{\partial \boldsymbol{\sigma}(t)^2}{\partial t} = 2 \mathbf{D}', \quad (9)$$

where \mathbf{D}' is the vectorial effective diffusion coefficient

$$\mathbf{D}' = \left(D + \lambda \frac{\sigma_x}{\sigma_y \sigma_z}, D + \lambda \frac{\sigma_y}{\sigma_x \sigma_z}, D + \lambda \frac{\sigma_z}{\sigma_x \sigma_y} \right), \quad (10)$$

with:

$$\lambda \equiv \frac{e N \mu}{20 \sqrt{5} \pi \epsilon}.$$

This effective diffusion coefficient encapsulates the effects of both diffusion and repulsion. At each time step, $\boldsymbol{\sigma}$ and \mathbf{D}' are recalculated and each charge element is displaced by a random walk in x , y , and z by distances selected from a Gaussian parameterized by $\sigma_i = \sqrt{2 D'_i \delta t}$, where δt is the size of the time step.

2.3.3. Trapping

While the charge carriers are moving in the detector, they may encounter impurities and recombine in the material, or are trapped and released on time scales longer than the shaping time of the readout electronics. When this occurs, we effectively lose the charge as it no longer contributes to the signal. We account for trapping by reducing the amount of charge present according to:

$$q(t) = q_0 e^{-t/\tau}, \quad (11)$$

where q_0 is the initial charge at time $t = 0$, t is the time since the energy was deposited, and τ is the carrier lifetime, which quantifies trapping as a bulk property of the cloud. The values of τ used in the simulations are listed in Table 1 with subscripts e and h electrons and holes, respectively. Trapping is caused by crystal defects such as Te precipitates (e.g. Bolke et al., 2017; Zhang et al., 2018; Winkler et al., 2019; Kim et al., 2019; Yakhimov et al., 2019; Brovko and Ruzin, 2020; McCoy et al., 2020). Owing to the lack of information about the spatial distribution and size of charge trapping sites, we neglect the statistical fluctuations caused by the charge trapping mechanisms. Detailed comparisons of simulations as those presented here and measured data could be used to constrain these material properties.

2.3.4. Charge integration

Charged particles moving near an electrode induce a charge on the electrode. Shockley showed a way to quantify this with the Shockley-Ramo Theorem (Shockley, 1938; He, 2001):

$$q_{ind} = -q \Delta \phi_{wp}, \quad (12)$$

where $\Delta\phi_{wp}$ is the change in weighting potential between two points in the charge q 's trajectory and q_{ind} is the charge induced on the electrode. The weighting potential is a unit-less potential found by setting the electrode for which we want to calculate the induced charge to 1 and all others to 0. With these boundary conditions, the procedure described in 2.2 is followed to calculate the weighting potential. The right panels of Figure 3 show that most of the change in weighting potential occurs near the pixels. This is the well-known small pixel effect (Barrett et al., 1995; He, 2001): as the signal is mostly generated near the pixels, it becomes largely independent of the location of the primary interaction.

To simulate the currents read by the electrodes, we use an alternate form of Eq. (12):

$$I_{ind} = q\mathbf{v} \cdot \mathbf{E}_{wp}, \quad (13)$$

where \mathbf{v} is the instantaneous velocity of the charge (considering both drift and diffusion) computed from the change of location in this time step, and \mathbf{E}_{wp} is the ‘‘electric field’’ resulting from the weighting potential. These are implemented as the average velocity over the whole time step and the trilinear interpolated weighting potential.

For each event, there may be several energy depositions following the initial photon interaction in the crystal, including elastic and inelastic photon scattering, and the ionization along the track of energetic electrons. Following the design of the HEXID ASIC, we assume that the electronics read out all pixels with an energy exceeding the trigger threshold as well as the immediate neighbors of these pixels (even if the signals in the neighboring pixels do not exceed the trigger threshold). We will see below that this scheme leads to excellent energy resolutions at lower photon energies ($< \sim 60$ keV). At higher energies, energy escaping the detector or traveling to pixels further away starts to become an issue, and does deteriorate the detectors' energy resolutions. We analyzed the data for the bipolar integration of the signal (read out of the integrated negative and positive charge).

3. Results

In this section, we discuss methods to reconstruct the energy of the incident photon, and the location of the primary interaction. We will first discuss the results obtained in the absence of readout noise, and the show how they change as we add the noise expected for the HEXID ASIC.

3.1. Energy reconstruction

The procedure in Section 2 was followed for a detector with the boundary conditions described in 2.2 and with 22.9 keV incident photons.

We characterize the amount of charge sharing with the charge ratio:

$$r = \frac{Q_{neighbors}}{Q_{center}}, \quad (14)$$

where Q_{center} is the charge induced on the center pixel (the pixel with the largest signal), and $Q_{neighbors}$ is the total charge induced

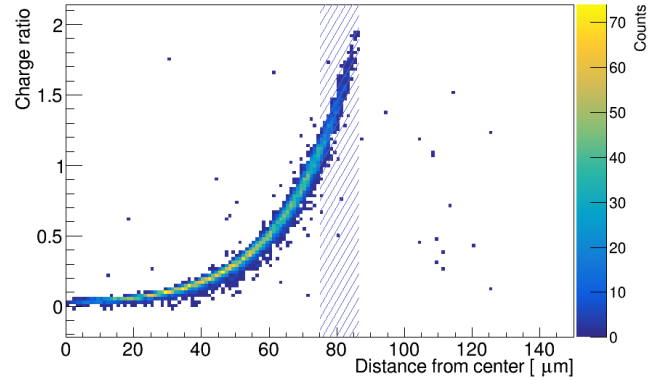


Figure 4: The panel shows the ratio r of the charge induced on neighbor pixels divided by the charge induced on the brightest pixel (Eq. (14)) as a function of the distance of the initial charge deposition from the center of the brightest pixel for incident 22.9 keV photons. The initial photon positions are randomized over a rectangular unit cell. Due to the hexagonal pixel geometry, the pixel edge may be located between $1/2$ and $1/\sqrt{3}$ pixel pitches from the center, indicated by the shaded area. As expected, there is more charge sharing as the interaction occurs farther from the pixel center.

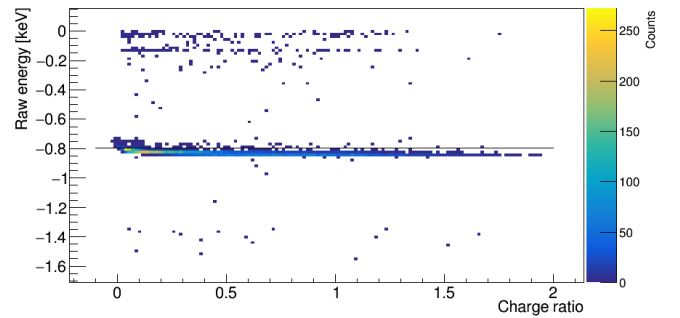


Figure 5: The total reconstructed charge for each event as a function of the charge ratio. The horizontal line indicates the expected total charge from a 22.9 keV incident photon. On average, there is more induced charge than expected. This small discrepancy may be due to the next layer of neighbors which were not considered; they are far enough that an opposite sign charge could have been induced, leading to more charge appearing to be induced within the nearest neighbors.

on its six neighbors. As expected, the charge ratio r increases with the distance from the center of the pixel (Fig. 4).

We see that adding up the charge from the center pixel which exceeds a certain threshold value and all its adjacent pixels is important for achieving good energy resolution. This requirement means that the total readout noise is given by the quadratic sum of the readout noise of a total of between one and seven pixels. Fig. 5 shows the total induced charge on the center pixel and its nearest neighbors plotted against the charge ratio. The sum signal decreases (increases in magnitude) with increasing charge ratio, which may be indicative of small negative induced charges from farther pixels for which the signal was not calculated.

To correct for this difference in charge, a multiplicative correction histogram was made from applying cuts at -0.6 and -1 fC to the plot in Fig. 5 and taking the average of the remaining points for each charge ratio bin. For each event, the recon-

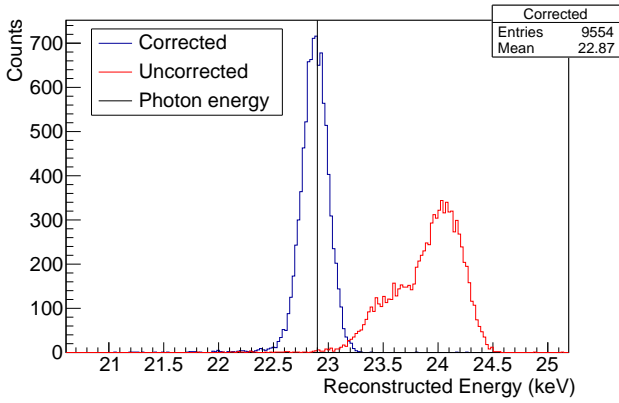


Figure 6: The reconstructed energies from the simulations for 22.9 keV incident photons. The red histogram shows the raw reconstructed energies inferred from summing the signal in the brightest pixel and its neighbors. The blue histogram shows the energies after correcting the signal with the charge ratio r from Equation (14). The black line indicates the incident photon energy.

reconstructed energy is corrected by multiplying the raw integrated charge by the value of this correction histogram corresponding to the event's charge ratio.

Figure 6 shows the energies reconstructed from charge integration both before and after multiplicative correction. The corrected peak has a full width at half maximum (FWHM) of 0.260 keV. The energy spectrum shown here does not yet include the electronic readout noise.

The readout Equivalent Noise Charge (ENC) depends on the detector capacitance and the readout electronics. The pixel capacitance can be calculated from two maps of the potential calculated for different bias voltages. Integrating the electric field around the pixel gives the charge on the pixel via Gauss' law. The difference ΔV of the two bias voltages and the difference Δq of the inferred charges gives the capacitance according to:

$$C = \frac{\Delta q}{\Delta V}. \quad (15)$$

For this 1 mm thick CZT detector with with 150 μm pixels, the per-pixel capacitance is 6.94 pF. For the HEXID architecture, this capacitance leads to a conservatively-estimated noise of 14-electron ENC. Figure 7 shows the results of the energy reconstruction with this noise included. The FWHM is 0.435 keV. The same correction histogram as before was used. The corrected energies' peak is still centered at the photon energy, which is expected given that the Gaussian was centered about 0, and that the noise is small compared to the total charge across all pixels, which contributes to minimal shifts in the charge ratio and therefore the correction factor.

We tested if a single correction histogram (derived for 22.9 keV photons) can be used to reconstruct the initial photon energy for a wide range of initial photon energies, i.e. 4.8 keV, 67.9 keV, and 78.4 keV. Figure 8 shows that a single correction histogram indeed gives excellent results for all these photon energies. For 4.8 keV photon events with noise, the corrected energy peak has a FWHM of 0.350 keV. For 67.9 keV and 78.4 keV photons, the corrected peak was slightly below

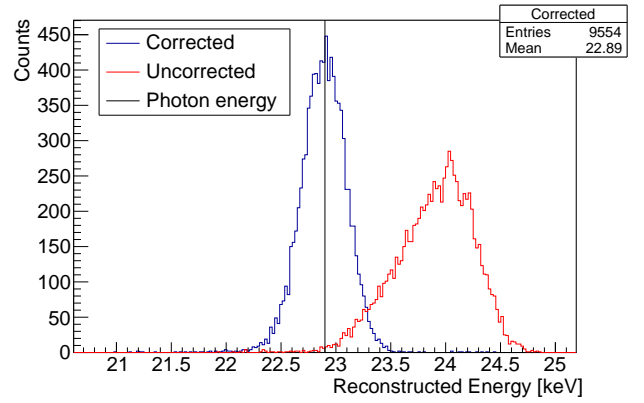


Figure 7: The reconstructed energies with a 14 electron ENC. The same correction histogram as that used for Fig. 6 was used.

Photon energy [keV]	Fano [keV]	Location Dependence [keV]	ENC [keV]	Total [keV]
4.8	0.104	0.017	0.334	0.350
22.9	0.228	0.125	0.349	0.435
67.9	0.398	0.376	0.607	0.815
78.4	0.421	1.014	0.756	1.333
122.1	0.525	3.995	2.421	4.701
158.4	0.598	7.818	0	7.841

Table 2: The resolution (FWHM) of the reconstructed energy from each source of noise: Fano noise, dependence of the induced charge on the locations of the energy deposition, electrical readout noise (ENC), and total noise. The 158.4 keV resolutions are calculated using twice the right-sided half width at half maximum due to high counts at low energies outside the photopeak. The contribution of ENC to the 158.4 keV peak resolution was not significant at the binning for which the peak was resolvable.

the incident photon energy. The reconstructed energies were multiplied by an additional correction factor to push the peak of the energy spectrum to the true X-ray energy. These factors were less than 1%, so they did not significantly impact the energy resolution. Note that the average values shown in the figures are lower than peak location due to the presence of the low-energy tails. The FWHM calculated from the binned spectra were 0.815 keV for the 67.9 keV incident photons and 1.333 keV for the 78.4 keV photons. The energy resolutions due to individual sources of noise are summarized in Table 2.

At even higher energies, the detector's performance starts to deteriorate markedly. Figure 9 shows simulated results for the 122.1 keV and 158.4 keV lines from ^{57}Co and ^{56}Ni , respectively. The energy spectra show pronounced low-energy tails. Two effects contribute to this effect: some of the photons interact close to the anode side of the detector, so that the drifting electrons induce little charge before impinging on the anodes (see Fig. 3, Eq. (12)). The second effect is that scattered photons are only absorbed after traveling beyond the next neighbor pixels, or leave the detector altogether. In both cases, their energy does not count towards the reconstructed

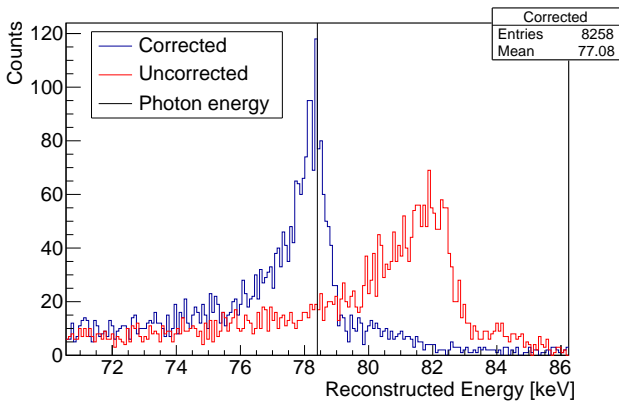
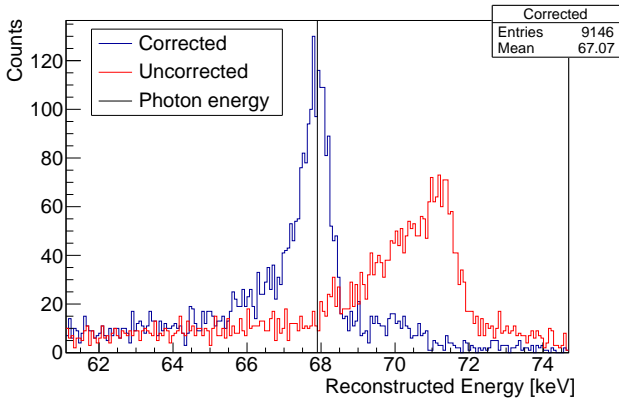
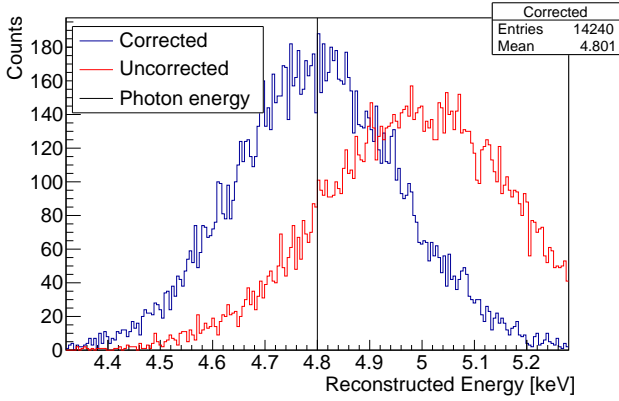


Figure 8: The reconstructed energies for 4.8 keV (*top*), 67.9 keV (*middle*), and 78.4 keV (*bottom*) photon events with 14-electron ENC. All used the correction histogram from the 22.9 keV simulations to correct the reconstructed energy based on the charge ratio and include a 14-electron ENC on each pixel. The 67.9 keV and 78.4 keV events were multiplied by an additional correction factor to center the peak in the incident photon energy without significantly impacting the energy resolution.

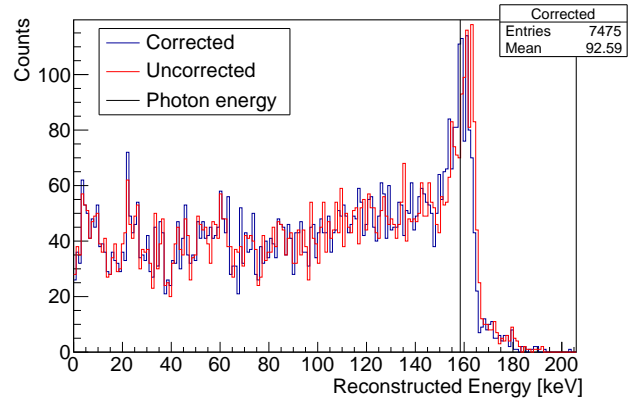
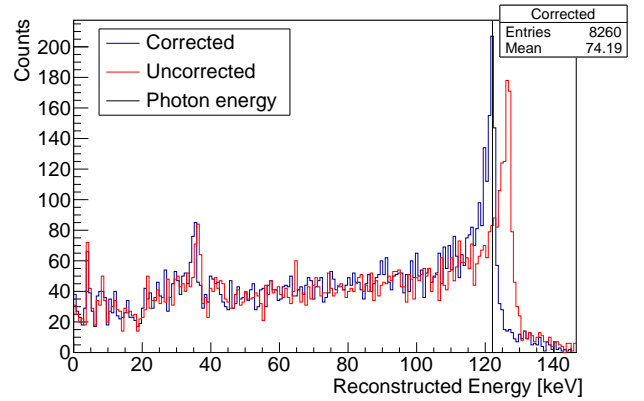


Figure 9: The reconstructed energies for 122.1 keV (*top*) and 158.4 keV (*bottom*) photon events with 14-electron ENC. There are significant energy losses as evidenced by the high level of reconstructed energies down to 0 keV. These reconstructed energies were multiplied by a small (~ 1) correction factor to shift the peak to the true photon energy.

energy. The 122.1 keV and 158.4 keV energy resolutions (including all effects) are 4.7 keV and 7.8 keV respectively (Table 2). At these high energies, the correction with the charge ratio r does not lead to a marked improvement of the energy resolutions. We therefore only used the raw integrated charge and a peak-shifting multiplicative factor close to one to reconstruct these energies. Developing and testing a more sophisticated Maximum Likelihood energy reconstruction is outside of the scope of this paper. Most photons do not interact with the detector at all; only 41% of 122.1 keV and 25% of 158.4 keV photons deposited any energy into the detector. Of these, 15% of 122.1 keV and 14% of 158.4 keV events resulted in reconstructed energies in the photopeak.

3.2. Position reconstruction

In the next step, we reconstruct the original photon position using the charge-weighted average position of the brightest pixel and its six nearest neighbors. The simulations include the readout noise of 14-electron ENC.

Figure 10 shows the absolute difference in the reconstructed x and y position of the incident photon using the weighted average of the pixels' center coordinates. We first discuss the results for 4.8 keV and 22.9 keV photons. There are clusters near

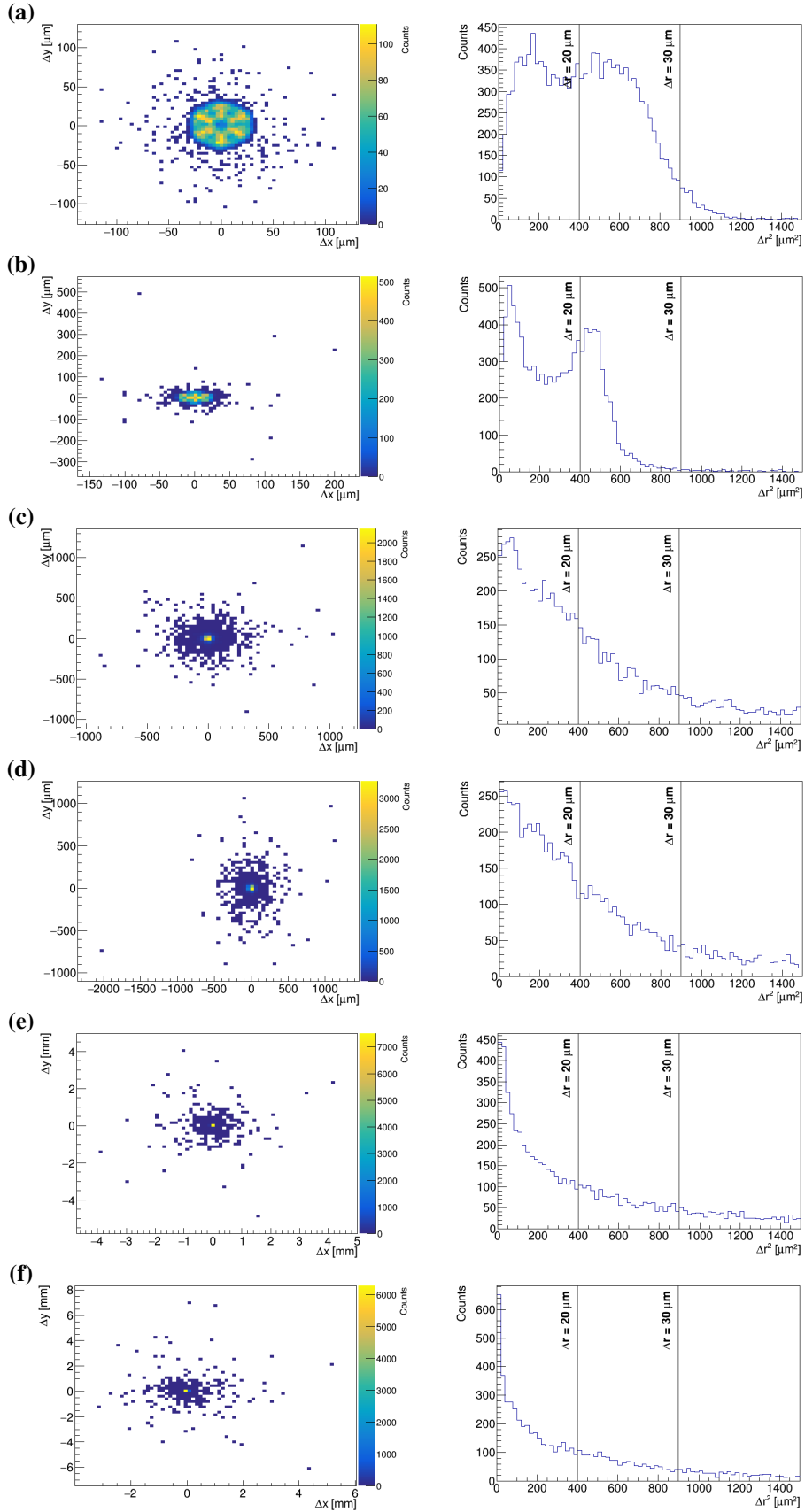


Figure 10: The absolute error in the reconstructed x and y position of the incident photon using the energy-weighted average of the integrated charge on the brightest pixel and its nearest neighbors (*left*) and the squared distance Δr^2 between the reconstructed position and incident photon (*right*) for 4.8 keV (a), 22.9 keV (b), 67.9 keV (c), 78.4 keV (d), 122.1 keV (e), and 158.4 keV (f) photons. Some reconstructed positions which are farther away from the main cluster may be due to effects from noise, as in the 4.8 keV case, and scattering in the higher energies. Lines are drawn at the locations of $\Delta r = 20 \mu\text{m}$ and $30 \mu\text{m}$.

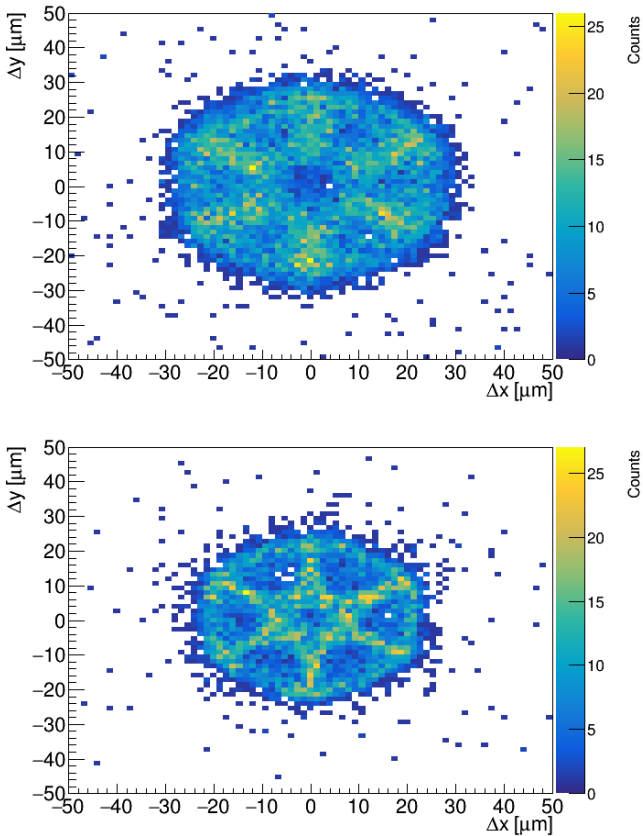


Figure 11: The errors in reconstructed photon positions for 4.8 keV (*top*) and 22.9 keV (*bottom*) zoomed to $\pm 50 \mu\text{m}$ in either direction. These account for over 99% of all reconstructed positions at these energies.

(0,0) for both energies that indicate that the reconstruction is generally accurate at these energies. In the reconstructions for both energies, there are a few reconstructed positions that are considerably farther away (>1 pixel pitch) from the actual photon position. We used simulations without ENC to prove that the main cause of this effect is the ENC for the 4.8 keV events and scattering for the 22.9 keV events. Note that the number of outliers is small. For the 22.9 keV events, 99.6% of the reconstructed positions are within $50 \mu\text{m}$ from the coordinates of the incident photon in both the x and y directions; for the 4.9 keV events, this number is 99.1%. Figure 11 zooms into this inner region and shows some interesting sub-structure.

The situation is somewhat different at higher energies (Fig. 10, lower four panels). The increased effect of charge sharing leads to a better position reconstruction for some events and thus to a more centrally peaked distance distribution. However, as scattered photons can travel farther away from the location of the first interaction, there is also a larger tail towards larger displacements. The net effect is that the HPD of the reconstructed positions is largely independent of the energy of the primary photon (Table 3).

Photon energy [keV]	Position Reconstruction HPD [μm]
4.8	41.8
22.9	34.5
67.9	43.4
78.4	41.0
122.1	46.4
158.4	37.7

Table 3: The spatial resolution (HPD) of the reconstructed positions from the simulated incident photons.

4. Discussion

In this paper, we present simulations of 1 mm thick CZT detectors with hexagonal pixels at an extremely small pixel pitch of $150 \mu\text{m}$. The detector simulations account for the spatially distributed generation of free charge carriers in the detector, and the drift and diffusion of the charge of both polarities. The simulations furthermore account for the anticipated charge resolution of the HEXID3 ASIC. We have shown that the sum of the signals of the brightest pixel and the adjacent pixels and the ratio of the sum of the charge in the neighbor pixel divided by the charge of the brightest pixel, give FWHM energy resolutions of 350 eV at 4.8 keV, 435 eV at 22.9 keV, 815 eV at 67.9 keV, 1.333 keV at 78.4 keV, 3.4 keV at 122.1 keV, and 9.8 keV at 158.4 keV. The charge induced on the brightest pixels and its neighbors can be used to reconstruct the location of the energy deposition to an accuracy of better than $50 \mu\text{m}$ for all the energies we simulated (4.8-158.4 keV). The simulations were performed using only the brightest pixel and its nearest neighbors to reflect the electronic readout scheme of the ASICs. The simulations described here have been used to optimize the design of readout ASICs which are currently in development at Brookhaven National Lab (Deptuch et al.). We plan to perform detailed comparison of simulated and measured data as soon as the first ASICs and detector/ASIC systems have been fabricated.

The results presented here can be compared with previously published simulated and experimental results. Benoit and Hamel (2009) for example simulate a 7.5 mm thick CZT detector with cross strip contacts at a pitch of $225 \mu\text{m}$ and obtain good agreement between simulated and experimental data. They report energy resolutions of approximately 7 keV and 14 keV FWHM for the 59.5 keV ^{241}Am line and 122.1 keV ^{57}Co line, respectively. The thick detectors suppress the low-energy tail evident in the energy spectra presented in this paper.

Ryan et al. (2017) present measurement results obtained with the HEXITEC CZT/ASIC hybrids which feature pixels at a next-neighbor pitch of $250 \mu\text{m}$ on 1 mm thick CZT detectors, and compare the experimental results with simulated results. Rather than modeling the spatially distributed energy depositions following the impact of the primary photon and the evolution of the charge cloud in the detector as done in our work, Ryan et al. used a phenomenological parameterization of the size of the charge clouds. Using a 2-D Gaussian with a width

$\sigma = 23 \mu\text{m}$, they were able to model the shape of the energy spectrum observed for a $\sim 20 \text{ keV}$ X-ray beam from an X-ray gun. Our approach is more general, and can be used over a wider range of energies.

The interested reader may consult (Iniewski et al., 2007; Rana et al., 2009; Kitaguchi et al., 2011; Yin et al., 2011, 2013, 2014; Veale et al., 2014; Montémont et al., 2014; Ocampo Giraldo et al., 2018; Khalil et al., 2018) for discussions of charge sharing in CZT detectors, and (Zhang et al., 2004; Benoit and Hamel, 2009; De Geronimo et al., 2008; Kim et al., 2011; Zhang et al., 2012; Beilicke et al., 2013; Yin et al., 2014; Kim et al., 2014; Wahl et al., 2015; Chen et al., 2018) for discussion of CZT detectors of different thicknesses and pixel sizes.

Detectors with pixels at $150 \mu\text{m}$ pixel pitch, as the ones discussed in this paper, would be well suited for a *NuSTAR* follow-up mission with arcsecond angular resolution and a *NuSTAR*-like focal length of 10 m. For these parameters, an HPD of $5''$ corresponds to a $242 \mu\text{m}$ focal spot. A pixel pitch of $150 \mu\text{m}$ would thus enable an oversampling factor of 1.6. A longer focal length of 20 m and an HPD of $15''$, as proposed for HEX-P (Madsen et al., 2018), the pixel diameter would correspond to a spot diameter of 1.5 mm, not necessitating sub-mm pixels.

At energies of $\sim 70 \text{ keV}$ and above, the 1 mm thick detectors studied in this paper start to become transparent, and the energy spectra start to develop an increasingly pronounced low-energy tail. The tail results from a combination of photons interacting close to the detector anodes so that electrons induce little charge before impinging on the anodes, and Compton scattered photons traveling beyond the next neighbor pixels or escaping the detector. Thicker detectors suppress both effects, but lead to longer drift paths and thus to additional charge spreading and larger pixel multiplicities – effects that adversely affect the energy resolution. Covering the broad energy range from $\sim 2 \text{ keV}$ to $\sim 160 \text{ keV}$ or higher as envisioned for *HEX-P* may require a layered detector, e.g. a front layer of thin ($\sim 1 \text{ mm}$) CZT detectors recording lower-energy photons with excellent energy and spatial resolutions, followed by a rear layer of thick ($\sim 1 \text{ cm}$) CZT detectors that catches the higher-energy photons with high efficiency and excellent resolutions.

Note that several alternatives to CZT detectors are currently being developed. A possible alternative for finely-pixelated CZT detectors are Thallium Bromide (TlBr) detectors. The high atomic number of Thallium (81) make TlBr more efficient for photoelectric interactions than CZT, and Kim et al. (2020) report sub-1% energy resolutions. Germanium based Charge Coupled Devices (Ge-CCDs) may be another competitor, but still suffer from yield issues (Leitz et al., 2019). We are currently evaluating the gamma-ray detectors made of tin absorbers and Transition Edge Sensors (TES) developed by the National Institute of Standards and Technology (NIST) (Bennett et al., 2012; Mates et al., 2017). The microcalorimeter detectors achieve superior energy resolutions (i.e. 53 eV at 97 keV) than solid state detectors. For the time being, the drawback of the TES gamma-ray detectors are spatial resolutions on the order of $\sim 1 \text{ mm}$.

Finely-pixelated CZT detectors as the ones discussed in this paper fill an important niche in the energy range of a few

keV to $\sim 100 \text{ keV}$ offering a unique combination of operation at room temperatures, high stopping power, high photo-electric to Compton scattering cross sections, sub-mm spatial resolutions, and good energy resolutions.

Acknowledgements

We thank Grzegorz Deptuch, Gabriella Carini, and Shaorui Li for their work on the HEXID ASIC, as well as the McDonnell Center for the Space Sciences at Washington University in St. Louis for its support. We thank Richard Bose and Andrew West for designing a HEXID readout system and HEXID photomasks. HK acknowledges NASA support under grants 80NSSC18K0264 and NNX16AC42G.

References

- Ariño-Estrada, G., Chmeissani, M., de Lorenzo, G., Kostein, M., Puigdemonges, C., García, J., Cabruja, E., 2014. Measurement of mobility and lifetime of electrons and holes in a schottky CdTe diode. *Journal of Instrumentation* 9, C12032–C12032. URL: <https://doi.org/10.1088/2F1748-0221/9/12/c12032>, doi:10.1088/1748-0221/9/12/c12032.
- Barrett, H.H., Eskin, J.D., Barber, H.B., 1995. Charge transport in arrays of semiconductor gamma-ray detectors. *Phys. Rev. Lett.* 75, 156–159. URL: <https://link.aps.org/doi/10.1103/PhysRevLett.75.156>, doi:10.1103/PhysRevLett.75.156.
- Baumgartner, W.H., Christe, S.D., Ryan, D.F., Inglis, A.R., Shih, A.Y., Gregory, K., Wilson, M., Seller, P., Gaskin, J., Wilson-Hodge, C., 2016. The HEXITEC hard x-ray pixelated CdTe imager for fast solar observations, in: Holland, A.D., Beletic, J. (Eds.), *High Energy, Optical, and Infrared Detectors for Astronomy VII*, p. 99151D. doi:10.1117/12.2234655.
- Beilicke, M., De Geronimo, G., Dowkontt, P., Garson, A., Guo, Q., Lee, K., Martin, J., Krawczynski, H., 2013. Performance of pixelated CZT detectors as a function of pixel and steering grid layout. *Nuclear Instruments and Methods in Physics Research A* 708, 88–100. doi:10.1016/j.nima.2013.01.016.
- Bennett, D.A., Horansky, R.D., Schmidt, D.R., Hoover, A.S., Winkler, R., Alpert, B.K., Beall, J.A., Doriese, W.B., Fowler, J.W., Fitzgerald, C.P., Hilton, G.C., Irwin, K.D., Kotsubo, V., Mates, J.A.B., O’Neil, G.C., Rabin, M.W., Reintsema, C.D., Schima, F.J., Swetz, D.S., Vale, L.R., Ullom, J.N., 2012. A high resolution gamma-ray spectrometer based on superconducting microcalorimeters. *Review of Scientific Instruments* 83, 093113–093113–14. doi:10.1063/1.4754630.
- Benoit, M., Hamel, L., 2009. Simulation of charge collection processes in semiconductor CdZnTe γ -ray detectors. *Nuclear Instruments and Methods in Physics Research Section A: Accelerators, Spectrometers, Detectors and Associated Equipment* 606, 508 – 516. URL: <http://www.sciencedirect.com/science/article/pii/S0168900209007864>, doi:<https://doi.org/10.1016/j.nima.2009.04.019>.
- Boggs, S.E., Harrison, F.A., Miyasaka, H., Grefenstette, B.W., Zoglauer, A., Fryer, C.L., Reynolds, S.P., Alexander, D.M., An, H., Barret, D., Christensen, F.E., Craig, W.W., Forster, K., Giommi, P., Hailley, C.J., Hornstrup, A., Kitaguchi, T., Koglin, J.E., Madsen, K.K., Mao, P.H., Mori, K., Perri, M., Pivovarov, M.J., Puccetti, S., Rana, V., Stern, D., Westergaard, N.J., Zhang, W.W., 2015. 44ti gamma-ray emission lines from sn1987a reveal an asymmetric explosion. *Science* 348, 670–671. URL: <https://science.sciencemag.org/content/348/6235/670>, doi:10.1126/science.aaa2259, arXiv:<https://science.sciencemag.org/content/348/6235/670.full.pdf>
- Bolke, J., O’Brien, K., Wall, P., Spicer, M., Gélinas, G., Beaudry, J.N., Alexander, W.B., 2017. Measuring Te inclusion uniformity over large areas for CdTe/CZT imaging and spectrometry sensors, in: *SPIE proceedings*, p. 104231M. doi:10.1117/12.2278584.
- Brovko, A., Ruzin, A., 2020. Study of material uniformity in high-resistivity $\text{Cd}_{1-x}\text{Zn}_x\text{Te}$ and $\text{Cd}_{1-x}\text{Mn}_x\text{Te}$ crystals. *Nuclear Instruments and Methods in Physics Research A* 958, 161996. doi:10.1016/j.nima.2019.03.051.

- CERN, 2019. Geant4. URL: <https://geant4.web.cern.ch/>.
- Chen, H., Li, H., Reed, M.D., Sundaram, A.G., Eger, J., Hugg, J.W., Abbaszadeh, S., Li, M., Montemont, G., Verger, L., Zhu, Y., He, Z., 2018. Development of large-volume high-performance monolithic CZT radiation detector, in: *Hard X-Ray, Gamma-Ray, and Neutron Detector Physics XX*, p. 107620N. doi:10.1117/12.2321244.
- De Geronimo, G., Vernon, E., Ackley, K., Dragone, A., Fried, J., O'Connor, P., He, Z., Herman, C., Zhang, F., 2008. Readout ASIC for 3D Position-Sensitive Detectors. *IEEE Transactions on Nuclear Science* 55, 1593–1603. doi:10.1109/TNS.2008.922217.
- Gaskin, J., Elsner, R., Ramsey, B., Wilson-Hodge, C., Tennant, A., Christie, S., Shih, A., Kilaru, K., Swartz, D., Seller, P., Wilson, M., Stuchlik, D., Weddendorf, B., 2015. Superhero: Design of a new hard-x-ray focusing telescope, in: *2015 IEEE Aerospace Conference*, pp. 1–15. doi:10.1109/AERO.2015.7119097.
- Grefenstette, B.W., Fryer, C.L., Harrison, F.A., Boggs, S.E., DeLaney, T., Laming, J.M., Reynolds, S.P., Alexander, D.M., Barret, D., Christensen, F.E., Craig, W.W., Forster, K., Giommi, P., Hailey, C.J., Hornstrup, A., Kitaguchi, T., Koglin, J.E., Lopez, L., Mao, P.H., Madsen, K.K., Miyasaka, H., Mori, K., Perri, M., Pivovarov, M.J., Puccetti, S., Rana, V., Stern, D., Westergaard, N.J., Wik, D.R., Zhang, W.W., Zoglauer, A., 2017. The Distribution of Radioactive ^{44}Ti in Cassiopeia A. *The Astrophysical Journal* 834, 19. doi:10.3847/1538-4357/834/1/19. arXiv:1612.02774.
- Grefenstette, B.W., Harrison, F.A., Boggs, S.E., Reynolds, S.P., Fryer, C.L., Madsen, K.K., Wik, D.R., Zoglauer, A., Ellinger, C.I., Alexander, D.M., An, H., Barret, D., Christensen, F.E., Craig, W.W., Forster, K., Giommi, P., Hailey, C.J., Hornstrup, A., Kaspi, V.M., Kitaguchi, T., Koglin, J.E., Mao, P.H., Miyasaka, H., Mori, K., Perri, M., Pivovarov, M.J., Puccetti, S., Rana, V., Stern, D., Westergaard, N.J., Zhang, W.W., 2014. Asymmetries in core-collapse supernovae from maps of radioactive ^{44}Ti in Cassiopeia A. *Nature* 506, 339–342. doi:10.1038/nature12997. arXiv:1403.4978.
- Harrison, F.A., Craig, W.W., Christensen, F.E., Hailey, C.J., Zhang, W.W., Boggs, S.E., Stern, D., Cook, W.R., Forster, K., Giommi, P., Grefenstette, B.W., Kim, Y., Kitaguchi, T., Koglin, J.E., Madsen, K.K., Mao, P.H., Miyasaka, H., Mori, K., Perri, M., Pivovarov, M.J., Puccetti, S., Rana, V.R., Westergaard, N.J., Willis, J., Zoglauer, A., An, H., Bachetti, M., Barrièrè, N.M., Bellm, E.C., Bhalerao, V., Brejnholt, N.F., Fuerst, F., Liebe, C.C., Markwardt, C.B., Nynka, M., Vogel, J.K., Walton, D.J., Wik, D.R., Alexander, D.M., Cominsky, L.R., Hornschemeier, A.E., Hornstrup, A., Kaspi, V.M., Madejski, G.M., Matt, G., Molendi, S., Smith, D.M., Tomsick, J.A., Ajello, M., Ballantyne, D.R., Baloković, M., Barret, D., Bauer, F.E., Blandford, R.D., Brandt, W.N., Brenneman, L.W., Chiang, J., Chakrabarty, D., Chenevez, J., Comastri, A., Dufour, F., Elvis, M., Fabian, A.C., Farrah, D., Fryer, C.L., Gothelf, E.V., Grindlay, J.E., Helfand, D.J., Krivonos, R., Meiner, D.L., Miller, J.M., Natalucci, L., Ogle, P., Ofek, E.O., Ptak, A., Reynolds, S.P., Rigby, J.R., Tagliaferri, G., Thorsett, S.E., Treister, E., Urry, C.M., 2013. The Nuclear Spectroscopic Telescope Array (NuSTAR) High-energy X-Ray Mission. *The Astrophysical Journal* 770, 103. doi:10.1088/0004-637X/770/2/103. arXiv:1301.7307.
- He, Z., 2001. Review of the Shockley-Ramo Theorem and its Application in Semiconductor Gamma-ray Detectors. *Nuclear Instruments and Methods in Physics Research, Section A: Accelerators, Spectrometers, Detectors and Associated Equipment* 463, 250–267. doi:10.1016/S0168-9002(01)00223-6.
- Iniewski, K., Chen, H., Bindley, G., Kuvvetli, I., Budtz-Jorgensen, C., 2007. Modeling charge-sharing effects in pixellated cztdetectors, in: *2007 IEEE Nuclear Science Symposium Conference Record*, pp. 4608–4611. doi:10.1109/NSSMIC.2007.4437135.
- Khalil, M., Dreier, E.S., Kehres, J., Jakubek, J., Olsen, U.L., 2018. Sub-pixel resolution in CdTe Timepix3 pixel detectors. *Journal of Synchrotron Radiation* 25, 1650–1657. URL: <https://doi.org/10.1107/S1600577518013838>, doi:10.1107/S1600577518013838.
- Kim, E., Kim, Y., Bolotnikov, A.E., James, R.B., Kim, K., 2019. Detector performance and defect densities in CdZnTe after two-step annealing. *Nuclear Instruments and Methods in Physics Research A* 923, 51–54. doi:10.1016/j.nima.2019.01.064.
- Kim, H., Ogorodnik, Y., Kargar, A., Cirignano, L., Thrall, C.L., Koehler, W., O'Neal, S.P., He, Z., Swanberg, E., Payne, S.A., Squillante, M.R., Shah, K., 2020. Thallium Bromide Gamma-Ray Spectrometers and Pixel Arrays. *Frontiers in Physics* 8, 55. doi:10.3389/fphy.2020.00055.
- Kim, J.C., Anderson, S.E., Kaye, W., Zhang, F., Zhu, Y., Kaye, S.J., He, Z., 2011. Charge sharing in common-grid pixelated CdZnTe detectors. *Nuclear Instruments and Methods in Physics Research A* 654, 233–243. doi:10.1016/j.nima.2011.06.038.
- Kim, J.C., Kaye, W.R., He, Z., 2014. Signal modeling of charge sharing effect in simple pixelated CdZnTe detector. *Journal of Korean Physical Society* 64, 1336–1345. doi:10.3938/jkps.64.1336.
- Kitaguchi, T., Grefenstette, B.W., Harrison, F.A., Miyasaka, H., Bhalerao, V.B., Cook, W.R., I., Mao, P.H., Rana, V.R., Boggs, S.E., Zoglauer, A.C., 2011. Spectral calibration and modeling of the NuSTAR CdZnTe pixel detectors. volume 8145 of *Society of Photo-Optical Instrumentation Engineers (SPIE) Conference Series*. p. 814507. doi:10.1117/12.896972.
- Krawczynski, H., Tueller, J., Barthelmy, S., Schnittman, J., Zhang, W., Krolik, J., Baring, M.G., Treister, E., Mushotzky, R., Beilicke, M., Buckley, J., Cowsik, R., Israel, M., 2012. The black hole evolution and space time (best) observatory. arXiv:1205.3691.
- Lai, X., Cai, L., Zimmerman, K., Kaul, M., Zhan, X., Qiang, Y., Veale, M., Thompson, R., 2019. CZT modeling for photon counting computer tomography, in: *SPIE proceedings*, p. 109484G. doi:10.1117/12.2512531.
- Leitz, C.W., Zhu, M., Rabe, S., Burke, B., Young, D., O'Mara, D., Prigozhin, I., Ryu, K., Cooper, M., Reich, R., Johnson, K., Cook, M., Stull, C., Zarr, S., 2019. Towards megapixel-class germanium charge-coupled devices for broadband x-ray detectors, in: *SPIE Proceedings*, p. 1111802. doi:10.1117/12.2528158.
- Li, S., De Geronimo, G., Fried, J., Pinelli, D.A., Kuczewski, A., Peter Siddons, D., Beheshtipour, B., Bohse, R., Krawczynski, H., 2017. Hexid2: A low-power, low-noise pixel readout asic for hyperspectral energy-resolving x-ray imaging detectors, in: *2017 IEEE Nuclear Science Symposium and Medical Imaging Conference (NSS/MIC)*, pp. 1–4. doi:10.1109/NSSMIC.2017.8533001.
- Li, S., De Geronimo, G., Giacomini, G., Fried, J., Pinelli, D.A., Singh, B., Miller, S., Nagarkar, V.V., 2018. Pd-hexid1: A low-power, low-noise pixel readout asic for pixelated-scintillator-based x-ray detectors, in: *2018 IEEE Nuclear Science Symposium and Medical Imaging Conference Proceedings (NSS/MIC)*, pp. 1–4. doi:10.1109/NSSMIC.2018.8824481.
- Madsen, K.K., Harrison, F., Broadway, D., Christensen, F.E., Descalle, M., Ferreira, D., Grefenstette, B., Gurgew, D., Hornschemeier, A., Miyasaka, H., Okajima, T., Pike, S., Pivovarov, M., Saha, T., Stern, D., Vogel, J., Windt, D., Zhang, W., 2018. Optical instrument design of the high-energy x-ray probe (HEX-P), in: *SPIE Proceedings*, p. 106996M. doi:10.1117/12.2314117.
- Mates, J.A.B., Becker, D.T., Bennett, D.A., Dober, B.J., Gard, J.D., Hays-Wehle, J.P., Fowler, J.W., Hilton, G.C., Reintsema, C.D., Schmidt, D.R., Swetz, D.S., Vale, L.R., Ullom, J.N., 2017. Simultaneous readout of 128 X-ray and gamma-ray transition-edge microcalorimeters using microwave SQUID multiplexing. *Applied Physics Letters* 111, 062601. doi:10.1063/1.4986222.
- McCoy, J.J., Kakkireni, S., Gélinas, G., Garaffa, J.F., Swain, S.K., Lynn, K.G., 2020. Effects of excess Te on flux inclusion formation in the growth of cadmium zinc telluride when forced melt convection is applied. *Journal of Crystal Growth* 535, 125542. doi:10.1016/j.jcrysgro.2020.125542.
- Montémont, G., Lux, S., Monnet, O., Stanchina, S., Verger, L., 2014. Studying spatial resolution of cztdetectors using sub-pixel positioning for spect. *IEEE Transactions on Nuclear Science* 61, 2559–2566. doi:10.1109/TNS.2014.2356293.
- Ocampo Giraldo, L., Bolotnikov, A.E., Camarda, G.S., De Geronimo, G., Fried, J., Gul, R., Hodges, D., Hossain, A., Ünlü, K., Vernon, E., Yang, G., James, R.B., 2018. Study of sub-pixel position resolution with time-correlated transient signals in 3D pixelated CdZnTe detectors with varying pixel sizes. *Nuclear Instruments and Methods in Physics Research A* 884, 136–139. doi:10.1016/j.nima.2017.12.024.
- Persson, M., Pelc, N.J., 2019. Simulation model for evaluating energy-resolving photon-counting CT detectors based on generalized linear-systems framework, in: *SPIE proceedings*, p. 109481V. doi:10.1117/12.2512593.
- Press, W.H., Flannery, B.P., Teukolsky, S.A., Vetterling, W.T., 2007. *Numerical Recipes*. Cambridge University Press.
- Rana, V.R., Cook, W.R., I., Harrison, F.A., Mao, P.H., Miyasaka, H., 2009. Development of focal plane detectors for the Nuclear Spectroscopic Telescope Array (NuSTAR) mission, in: *Siegmund, O.H. (Ed.), UV, X-Ray, and Gamma-Ray Space Instrumentation for Astronomy XVI*, p. 743503. doi:10.1117/12.825418.
- Redus, R.H., Pantazis, J.A., Huber, A.C., Jordanov, V.T., Butler, J.F., Apo-

- ovsky, B., 1997. Fano factor determination for czts. *MRS Proceedings* 487, 101. doi:[10.1557/PROC-487-101](https://doi.org/10.1557/PROC-487-101).
- Ryan, D., Christe, S., Shih, A., Inglis, A.R., Gregory, K., Baumgartner, W.H., Gaskin, J., Wilson-Hodge, C., Seller, P., Wilson, M., Veale, M.C., Panessa, M., 2016. HEXITEC: A Next Generation Hard X-ray Detector for Solar Observations, in: *AAS/Solar Physics Division Abstracts #47*, p. 8.11.
- Ryan, D.F., Christe, S.D., Shih, A.Y., Baumgartner, W.H., Wilson, M.D., Seller, P., Gaskin, J.A., Inglis, A., 2017. Modeling and measuring charge sharing in hard x-ray imagers using HEXITEC CdTe detectors, in: *Society of Photo-Optical Instrumentation Engineers (SPIE) Conference Series*, p. 1039702. doi:[10.1117/12.2274419](https://doi.org/10.1117/12.2274419).
- Shockley, W., 1938. Currents to Conductors Induced by a Moving Point Charge. *Journal of Applied Physics* 9, 635–636. doi:[10.1063/1.1710367](https://doi.org/10.1063/1.1710367).
- Veale, M.C., Bell, S.J., Duarte, D.D., Schneider, A., Seller, P., Wilson, M.D., Iniewski, K., 2014. Measurements of charge sharing in small pixel CdTe detectors. *Nuclear Instruments and Methods in Physics Research A* 767, 218–226. doi:[10.1016/j.nima.2014.08.036](https://doi.org/10.1016/j.nima.2014.08.036).
- Wahl, C.G., Kaye, W.R., Wang, W., Zhang, F., Jaworski, J.M., King, A., Boucher, Y.A., He, Z., 2015. The Polaris-H imaging spectrometer. *Nuclear Instruments and Methods in Physics Research A* 784, 377–381. doi:[10.1016/j.nima.2014.12.110](https://doi.org/10.1016/j.nima.2014.12.110).
- Winkler, A., Naaranoja, T., Gädda, A., Ott, J., Luukka, P., Karadzhinova-Ferrer, A., Kalliokoski, M., Härkönen, J., 2019. Optical and electrical characterization of Cadmium Telluride X-ray pad detectors. *Nuclear Instruments and Methods in Physics Research A* 924, 28–32. doi:[10.1016/j.nima.2018.08.032](https://doi.org/10.1016/j.nima.2018.08.032).
- Wohl, C.G., Cahn, R.N., Rittenberg, A., Trippe, T.G., Yost, G.P., Porter, F.C., Hernandez, J.J., Montanet, L., Hendrick, R.E., Crawford, R.L., Roos, M., Törnqvist, N.A., Höhler, G., Aguilar-Benitez, M., Shimada, T., Losty, M.J., Gopal, G.P., Walck, C., Shrock, R.E., Frosch, R., Roper, L.D., Trower, W.P., Armstrong, B. (Particle Data Group), 1984. Review of particle properties. *Rev. Mod. Phys.* 56, S1–S299. URL: <https://link.aps.org/doi/10.1103/RevModPhys.56.S1>, doi:[10.1103/RevModPhys.56.S1](https://doi.org/10.1103/RevModPhys.56.S1).
- Yakimov, A., Smith, D., Choi, J., Araujo, S., 2019. Growth and characterization of detector-grade CdZnTeSe by horizontal Bridgman technique, in: *SPIE proceedings*, p. 111141N. doi:[10.1117/12.2528542](https://doi.org/10.1117/12.2528542).
- Yin, Y., Chen, X., Li, C., Wu, H., Komarov, S., Guo, Q., Krawczynski, H., Meng, L.J., Tai, Y.C., 2014. Evaluation of PET Imaging Resolution Using 350 μm Pixelated CZT as a VP-PET Insert Detector. *IEEE Transactions on Nuclear Science* 61, 154–161. doi:[10.1109/TNS.2013.2294011](https://doi.org/10.1109/TNS.2013.2294011).
- Yin, Y., Chen, X., Wu, H., Komarov, S., Garson, A., Li, Q., Guo, Q., Krawczynski, H., Meng, L.J., Tai, Y.C., 2013. 3-d spatial resolution of 350 μm pitch pixelated cdznte detectors for imaging applications. *IEEE Transactions on Nuclear Science* 60, 9–15. doi:[10.1109/TNS.2012.2213611](https://doi.org/10.1109/TNS.2012.2213611).
- Yin, Y., Chen, X., Wu, H., Komarov, S., Lee, K., Guo, Q., Krawczynski, H., Tai, Y., 2011. Resolution improvement by interpolation of charge sharing event position in 350 μm pitch pixelated cdznte detectors, in: *2011 IEEE Nuclear Science Symposium Conference Record*, pp. 3263–3266. doi:[10.1109/NSSMIC.2011.6152587](https://doi.org/10.1109/NSSMIC.2011.6152587).
- Zhang, F., He, Z., Xu, D., 2004. Analysis of Detector Response Using 3-D Position-Sensitive CZT Gamma-Ray Spectrometers. *IEEE Transactions on Nuclear Science* 51, 3098–3104. doi:[10.1109/TNS.2004.839078](https://doi.org/10.1109/TNS.2004.839078).
- Zhang, F., Herman, C., He, Z., De Geronimo, G., Vernon, E., Fried, J., 2012. Characterization of the H3D ASIC Readout System and 6.0 cm^3 3-D Position Sensitive CdZnTe Detectors. *IEEE Transactions on Nuclear Science* 59, 236–242. doi:[10.1109/TNS.2011.2175948](https://doi.org/10.1109/TNS.2011.2175948).
- Zhang, S., Wang, C., Zhao, B., Zhang, H., Zheng, L., 2018. Controlling Te inclusion during direct mixed solution growth of large size CdZnTe crystal, in: *SPIE proceedings*, p. 107620V. doi:[10.1117/12.2327047](https://doi.org/10.1117/12.2327047).
- Zhang, W.W., Allgood, K.D., Biskach, M.P., Chan, K.W., Hlinka, M., Kearney, J.D., Mazzarella, J.R., McClelland, R.S., Numata, A., Riveros, R.E., Saha, T.T., Solly, P.M., 2018. Astronomical x-ray optics using mono-crystalline silicon: high resolution, light weight, and low cost, in: den Herder, J.W.A., Nikzad, S., Nakazawa, K. (Eds.), *Space Telescopes and Instrumentation 2018: Ultraviolet to Gamma Ray*, International Society for Optics and Photonics. SPIE. pp. 130 – 139. URL: <https://doi.org/10.1117/12.2312879>, doi:[10.1117/12.2312879](https://doi.org/10.1117/12.2312879).